

Robust segmented entangling gates with pulse gradient and power optimization using a hypersurface-tangent method

Lin Cheng ^{1,4} Sheng-Chen Liu ¹ Lei Geng ¹ Yong-Kang Fang ¹ and Liang-You Peng ^{1,2,3,4,*}

¹*State Key Laboratory for Mesoscopic Physics and Frontiers Science Center for Nano-Optoelectronics, School of Physics, Peking University, Beijing 100871, China*

²*Collaborative Innovation Center of Quantum Matter, Beijing 100871, China*

³*Collaborative Innovation Center of Extreme Optics, Shanxi University, Taiyuan 030006, China*

⁴*Beijing Academy of Quantum Information Sciences, Beijing 100193, China*



(Received 1 January 2023; accepted 5 April 2023; published 24 April 2023)

To implement a scalable and fault-tolerant programmable quantum computing architecture, the realization of high-fidelity, robust, and efficient quantum entangling gates in a multiqubit system is an essential requirement. In this paper, we consider the optimization of the segmented amplitude-modulated entangling gates realized by applying spin-dependent forces to a chain of ions trapped in a hybrid quadratic and quartic potential. We propose a geometrical hypersurface-tangent method to optimize the laser power and the pulse gradient, carefully considering the experimental feasibility in realizing the effective Rabi frequency and its change between adjacent pulse segments. In addition, our method allows us to optimize the solution for the case of a few segments by constructing an approximated null space through trading a negligible amount of gate fidelity. Finally, we show that the present scheme can provide a unified framework to improve the robustness to an arbitrary order against random static drifts of the motional frequencies, the gate duration errors, the laser detuning drifts, and their simultaneous drifts.

DOI: [10.1103/PhysRevA.107.042617](https://doi.org/10.1103/PhysRevA.107.042617)

I. INTRODUCTION

Quantum computers are expected to solve certain problems much better than any possible classical computers, such as the factorization of a large number and the simulation of quantum many-body systems. In recent years, researchers have made significant progress toward building a practical quantum computer by utilizing various physical platforms such as trapped ions [1–4], superconducting qubits [5–9], photons [10], cold atoms [11,12], topological quantum computation [13], and others [14]. Since it was first proposed in 1995 [15], the trapped-ion system is one of the most promising platforms for large-scale quantum computing due to many beneficial characteristics, such as the longest coherence time of the single qubit [16], the nearly perfect initialization and detection scheme [17,18], the high-fidelity quantum gates [19–21], and the wonderful qubit connectivity. Among the most important issues, entangling quantum gates have recently been the focus of many theoretical and experimental investigations, which aim at improving the fidelity, the efficiency, and the robustness. For example, fidelities higher than 99.99% for single-qubit gates and 99.9% for two-qubit entangling gates have been reported [19–21]. Meanwhile, some important quantum algorithms, such as Shor’s algorithm and the quantum error correction, have been demonstrated on a small programmable quantum computer [22–24].

However, while state-of-the-art ion traps can confine one-dimensional chains of more than a hundred ions, scaling up and, in particular, gate operations in a long chain are challenging. For a small number of ions, the Mølmer-Sørensen gate [25–27] utilizes a single phonon mode of the ion crystal which serves as a data bus for the transmission of quantum information to mediate the coupling between two ions’ internal states. However, the motional modes become progressively dense for a long chain, which means that gate operations that rely on using a single phonon mode become slow due to the necessity to spectrally resolve this mode. Moreover, the crosstalk, i.e., unwanted interactions among different modes, can lead to significant errors in the quantum gates. The problem may be mitigated by shuttling ions between separate trapping zones, a scheme named the quantum charge-coupled device [28]. However, it demands an exquisite control of ion positions and even in that architecture it will be meaningful to increase the number of qubits per zone.

In this paper, we will follow an alternative approach, where the spin-dependent driving optical forces can simultaneously couple to all motional modes to address the scaling problem [29–31]. The suppression of modes crosstalk provides a high fidelity without slowing down the gate. The requirements of disentangling the internal qubit states from all motional modes can be readily achieved via modulating experimental parameters with a high tunability. A number of schemes have been proposed such as the modulation of the amplitude [29–32], the frequency [33–35], or the phase [36–38] of the driving laser fields, as well as their combinations [39–42]. Each of these methods has been proposed and implemented in a

*liangyou.peng@pku.edu.cn

discrete or continuous way in a multiqubit system [38,43–45]. Specifically, we adopt the laser amplitude modulation for the scalable entanglement, which has been theoretically proposed [29] and experimentally demonstrated in a five-ion system [43]. The segmented laser amplitudes are carefully designed to decouple the internal qubit states from all the motional modes and generate a maximal spin-spin entangling gate.

In previous work, for N trapped ions, segments fewer than $2N + 1$ were used to achieve high-fidelity entangling gates by scanning the experiment parameters (such as the gate duration and the laser detuning) where $2N + 1$ is the number of constraints [29–32]. In appropriate experiment parameters, the fidelity of the quantum gate is very close to an ideal operation. However, the solution may not be efficient with respect to the large Rabi frequency or the sharp variation of the pulse shape, as the laser amplitudes are equally segmented in discrete time intervals and abrupt changes in laser amplitudes are hard to be physically realized, especially when one performs the fast gates. We refer to the amplitude change between any two adjacent segments of the pulse as the pulse gradient. In addition, the optical components in trapped-ion experiments can only withstand limited laser power. More importantly, an increased laser power can reduce the gate fidelity due to the spontaneous emission, the ion-ion crosstalk, etc. Therefore, in addition to pursuing high fidelity, it is important to reduce the pulse gradient and achieve the least amount of laser power.

In this paper, we will present a comprehensive approach to the construction of high-fidelity and robust quantum gates with the optimization of the laser power and the pulse gradient. For such purposes, we propose a geometrically hypersurface-tangent method to obtain the optimized combination of vectors of the null space. Considering a few segments of pulse in which case there does not exist the null space, based on the tradeoff method with modulating the amplitude and the frequency simultaneously in a continuous way for ideal operation (see Ref. [46]), we can construct an approximated null space (ANS) at the cost of a negligible amount of the gate fidelity to reduce the laser power or to achieve a more smooth pulse shape.

Finally, it is also important to construct gates being stabilized against control parameter fluctuations, such as mode frequency fluctuations, trap anharmonicities, pulse timing errors, and the heating and optical phase noises. Recently, several gates with an increased robustness against different errors have been proposed and demonstrated with multiple ions [33,36,41,42]. We present a linear approach designed to suppress the dominant source of infidelity, which is related to the residual entanglement between the motional modes and the internal qubit states. The stabilization condition can be linearly expressed with the laser amplitude, which lends itself naturally to the method of constructing pulses. We demonstrate that it is possible to design quantum entangling gates that are robust against the gate duration errors, the random static drifts of motional frequencies, the laser detuning drifts, or the mixture of them.

The rest of this paper is organized as follows: In Sec. II, we give a brief introduction of the phase-insensitive $\sigma_{\phi_s}, \sigma_{\phi_x}$ entangling gates between any pair of ions in a long ion chain. In Sec. III, we will introduce in detail the optimization scheme to achieve the efficient quantum gates with a high fidelity

and robustness for different pulse segments, especially the present geometrically hypersurface-tangent method. And in Sec. IV, we will discuss the results of quantum gates in a chain of 20 $^{171}\text{Yb}^+$ ions. We present the optimized results of the laser power and the pulse shape for different pulse segments. Particularly, we will compare the exact method and the approximated (extended) null space method to show the tradeoff advantage. The robustness of the quantum gates under experimental fluctuations will be then discussed. At the end of this section, we will discuss the scaling behavior of the gate construction with the system size. Finally, we will summarize our main results in Sec. V.

II. THEORETICAL MODEL

For N ions in a linear Paul trap along the axial direction, a suitable hybrid potential consisting of a quadratic and quartic term can be applied in the axial direction through external electrodes to achieve a uniform configuration [31,32,47,48]. The static equilibrium configuration can be determined by a balance between the axial confining fields and the mutual Coulomb repulsion. For typical experimental parameters, the micromotion is small and can be usually neglected. Specifically, one can obtain the motional modes and their corresponding mode frequencies through the diagonalization of the symmetric Hessian matrix of the total potential energy [49,50], whose details can be found in Appendix A.

In this section, we present a brief introduction of the entangling quantum gates which are mediated by the collective phonon modes of motion through spin-dependent optical forces. In the present paper, we mainly focus on the phase-insensitive $\hat{\sigma}_{\phi_s}, \hat{\sigma}_{\phi_x}$ gate [51,52], where $\hat{\sigma}_{\phi_s} = \cos \phi_s \hat{\sigma}_x + \sin \phi_s \hat{\sigma}_y$ with $\hat{\sigma}_x$ and $\hat{\sigma}_y$ being the Pauli operators. The optical forces are realized by shining two counterpropagating beams on the ions, with an equal but opposite detuning μ in the neighborhood of the motional mode frequencies. The interaction Hamiltonian of the system takes a general form [32] as

$$H_I = \sum_{j=1}^N \hbar \Omega_j(t) \cos[\mu t + \phi_m^j - \Delta k q_j(t)] \hat{\sigma}_{\phi_s^j}^j, \quad (1)$$

where $\Omega_j(t)$ denotes the two-photon Rabi frequency of the j th ion, which is proportional to the intensity of the driving laser, $\Delta k = |\mathbf{k}_2 - \mathbf{k}_1|$ is the difference of two wave vectors, $\hat{\sigma}_{\phi_s^j}^j$ is the Pauli spin-flip operator for the j th ion, and $\phi_s^j = (\Delta\varphi_b^j + \Delta\varphi_r^j)/2$ and $\phi_m^j = (\Delta\varphi_b^j - \Delta\varphi_r^j)/2$ are called the spin phase and the motional phase [32].

The transverse displacement q_j of the j th ion can be quantized as

$$q_j(t) = \sum_m b_j^m \sqrt{\frac{\hbar}{2m_{\text{ion}}\omega_m}} (\hat{a}_m e^{-i\omega_m t} + \hat{a}_m^\dagger e^{i\omega_m t}), \quad (2)$$

where \hat{a}_m^\dagger and \hat{a}_m are respectively the creation and the annihilation operator acting on the m th motional mode, b_j^m is the motional mode eigenvector for the j th ion and the m th mode with ω_m being its mode frequency, and m_{ion} is the mass of a single ion. The summation over m is limited to the transverse modes along the x direction in our calculations.

By using the rotating wave approximation in the Lamb-Dicke and resolved-sideband limits, the time evolution operator of the interaction Hamiltonian can be obtained via the Magnus expansion

$$\hat{U}(\tau) = \exp \left\{ \sum_{j,m} (\alpha_j^m(\tau) \hat{a}_m^\dagger - \alpha_j^{m*}(\tau) \hat{a}_m) \hat{\sigma}_{\phi_s}^j + i \sum_{i < j} \theta_{ij}(\tau) \hat{\sigma}_{\phi_s}^i \hat{\sigma}_{\phi_s}^j \right\}, \quad (3)$$

where

$$\alpha_j^m(\tau) = -i \eta_j^m \int_0^\tau \Omega_j(t) \sin[\mu t + \phi_m^j(t)] e^{i\omega_m t} dt, \quad (4)$$

$$\begin{aligned} \theta_{ij}(\tau) = & 2 \sum_m \eta_i^m \eta_j^m \int_0^\tau dt_2 \int_0^{t_2} dt_1 \Omega_i(t_2) \Omega_j(t_1) \\ & \times \sin[\mu t_1 + \phi_m^i(t_1)] \sin[\mu t_2 + \phi_m^j(t_2)] \\ & \times \sin[\omega_m(t_1 - t_2)], \end{aligned} \quad (5)$$

in which $\alpha_j^m(\tau)$ describes the residual decoupling between the internal qubit state of the j th ion and the m th motional mode corresponding to the residual spin-dependent displacements in the phase space at the gate duration τ . The coupling strength $\theta_{ij}(\tau)$ between the i th and the j th qubit corresponds to the accumulated phase. The Lamb-Dicke parameter $\eta_j^m = b_j^m \Delta k \sqrt{\frac{\hbar}{2m_{\text{ion}}\omega_m}}$ couples the j th ion with the m th mode.

For a successful completion of an entangling operation, the qubit states should be completely decoupled from all motional modes, which means that the phase-space trajectories of all motional modes return to their origins. Meanwhile, the qubit states should undergo a maximal entanglement of $\pi/4$ at the end of the gate duration. Mathematically, the following conditions should be satisfied:

$$\alpha_j^m(\tau) = 0, \quad \forall j, \forall m, \quad (6)$$

$$\theta_{ij}(\tau) = \pm \pi/4. \quad (7)$$

Therefore, for an ideal gate, the evolution operator reaches $U_{ij} = \exp(\pm i\pi \hat{\sigma}_{\phi_s}^i \hat{\sigma}_{\phi_s}^j / 4)$.

Let us consider a general situation with an N_1 -qubit entangling quantum gate in an N -ion chain which utilizes N collective transverse modes. At the end of the gate operation, for the N_1 ions involved and N transverse modes, the $N_1 \times N$ displacement values in Eq. (4) should vanish, which means that all motional modes trajectories should be closed in the phase space. Thus, there are $2N_1 \times N$ constraints because of the complex properties of Eq. (4). One requires that $\theta_{ij} = \pm \pi/4$ for each desired pair of entangled ions at the maximal entanglement, and for the others $\theta_{ij} = 0$, whose interactions represent the crosstalk. Therefore, a total number of $2N_1 \times N + N_1(N_1 - 1)/2$ constraints should be satisfied for implementing N_1 -qubit high-fidelity parallel entangling gates.

Up to this point, the above analysis is quite general: any pulse parameters can be optimized to satisfy the above constraints and improve the robustness against some common experimental errors. In previous studies, amplitude-modulated (AM) gates [29–32], phase-modulated (PM) gates [36–38], frequency-modulated (FM) gates [33–35], and their

combinations [39–42] have been developed and demonstrated in a discrete or continuous way. The fidelity of the AM, PM, and FM gates demonstrated in a chain of five (or more) ions is around 97–99.9%, when transverse motional modes are used for the gates [38,43–45].

According to Ref. [32], we can use the average gate fidelity to measure the gate performance:

$$\bar{F} = \frac{1}{10} [4 + 2(\Gamma_i + \Gamma_j) \sin |2\theta_{ij}| + \Gamma_+ + \Gamma_-], \quad (8)$$

where

$$\Gamma_{i(j)} = \exp \left[-2 \sum_m |\alpha_{i(j)}^m|^2 \coth \left(\frac{\hbar\omega_m}{2k_B T} \right) \right], \quad (9)$$

$$\Gamma_{\pm} = \exp \left[-2 \sum_m |\alpha_i^m \pm \alpha_j^m|^2 \coth \left(\frac{\hbar\omega_m}{2k_B T} \right) \right]. \quad (10)$$

In the limit of small $\alpha_j^m(\tau)$ and $\alpha_i^m(\tau)$, which means a high fidelity, the average infidelity can be approximated as

$$\delta \bar{F}_a \approx 1 - F_a = \frac{4}{5} \sum_m (|\alpha_i^m|^2 + |\alpha_j^m|^2) (2\bar{n}_m + 1), \quad (11)$$

which is used in the robustness calculations later with \bar{n}_m being the averaged phonon number of the m th mode.

III. OPTIMIZED ROBUST GATES

In this paper, we focus on the discrete AM gates and propose a very efficient linear method to design an optimized and robust entangling gate with a high fidelity for an arbitrary pair of qubits in the trapped-ion quantum computer. In addition to the power optimization, which has been previously discussed in many contexts [41,42], we propose a hypersurface-tangent method to optimize the pulse gradient, that is, to minimize the intensity change of two adjacent segments of the pulse. Additionally, we will apply our optimized scheme to the case of a few pulse segments, whose parameters are readily feasible in experiments, by the tradeoff method proposed in Ref. [46]. We show that one can construct an approximated null space to reduce the laser power or the pulse gradient at the cost of a negligible loss of the gate fidelity. We will also demonstrate the improvement of the robustness against various types of external parameter drifts to an arbitrary order at a cost linear with respect to the order. Examples will be given to gate duration errors, random drifts of motional frequencies, the laser detuning drifts, and the mixed drifts of them.

A. Equations of main constraints

In this paper, we will focus on a two-qubit quantum gate in a chain of 20 ions. We assume that the intensities of the driving fields are equal for the two ions, which can be easily realized in experiments. Without loss of generality, one can choose $\phi_s = \phi_m^j = \phi_m^i = 0$. Note that the Rabi frequency can be allowed to take negative values by adding a phase shift of π . However, we tend to obtain results in which all the Rabi frequencies are positive for the pulse gradient optimization. This yields a total of $2N + 1$ constraints for designing appropriate discrete pulse sequences $\mathbf{\Omega}(\tau)$, i.e., one accumulated phase condition and $2N$ spin-motion decoupling conditions.

To fulfill these constraints and provide an optimal control, we divide the total gate interval τ into N_{seg} segments with an equal time duration of τ/N_{seg} . Let the Rabi frequency be a constant in each segment and treat the amplitude in each segment as an independent variable. Thus, we define a real column vector $\boldsymbol{\Omega} = (\Omega_1, \Omega_2, \dots, \Omega_{N_{\text{seg}}})^T$, corresponding to the Rabi frequency of each segment.

The $2N$ spin-motion decoupling constraints in Eq. (6) and the accumulated phase constraint in Eq. (7) can respectively be written in a matrix form as follows:

$$\mathbf{M}\boldsymbol{\Omega} = \mathbf{0}, \quad (12)$$

$$\boldsymbol{\Omega}^T \mathbf{S} \boldsymbol{\Omega} = \theta_{ij}, \quad (13)$$

where \mathbf{M} is the $2N \times N_{\text{seg}}$ coefficient matrix, \mathbf{S} is the $N_{\text{seg}} \times N_{\text{seg}}$ matrix, and $\boldsymbol{\Omega}$ is the amplitude vector of length N_{seg} . Since θ_{ij} is a scalar, we can further construct a symmetric matrix $\mathbf{D} = (\mathbf{S} + \mathbf{S}^T)/2$ such that $\theta_{ij} = \boldsymbol{\Omega}^T \mathbf{S} \boldsymbol{\Omega} = \boldsymbol{\Omega}^T \mathbf{D} \boldsymbol{\Omega}$. The explicit expressions of \mathbf{M} and \mathbf{S} are given in Appendix B. As can be seen, the $2N$ spin-motion decoupling constraints are linear with respect to the control laser parameters, while the accumulated phase constraint is quadratic.

B. Additional constraints under the consideration of robustness

In addition to ensuring that all excited modes are decoupled under ideal operating conditions, we also require that the entangling gate operation be robust against various types of external parameters errors. Here, we demonstrate that our optimization method is robust against the gate duration errors, random drifts of motional frequencies, the laser detuning errors, and the mixed drifts of them. According to the definition of fidelity in Eq. (8), the residual coupling of qubit internal states to multiple motional modes has a greater impact on the fidelity of the quantum gate. By suitably scaling $\boldsymbol{\Omega}$, one can always achieve $\theta_{ij} = \pm\pi/4$. Therefore, we can improve the robustness of the quantum gate by requiring the residual coupling α_j^m be stationary up to the n th order with respect to variations in parameters.

In experiments, the motional-mode frequencies ω_m can drift due to some uncontrollable effects, such as stray electromagnetic fields. Thus, one requires that

$$\frac{\partial^k \alpha_j^m}{\partial \omega_m^k} = 0, \quad m = 1, \dots, N, \quad (14)$$

or, in matrix notation,

$$\mathbf{K}_m^{(k)} \boldsymbol{\Omega} = \mathbf{0}, \quad (15)$$

where $\mathbf{K}_m^{(k)}$ is the $2N \times N_{\text{seg}}$ coefficient matrix including the stabilization of the m th motional mode and the j th ion against drifts to an arbitrary stabilization order $k = 1, \dots, K_\omega$. Since the calculation of every motional mode is independent, one can achieve stabilization against random static fluctuations (i.e., individual mode drifts) independently.

Similarly, to stabilize against gate duration errors, one requires

$$\frac{\partial^l \alpha_j^m}{\partial \tau^l} = 0, \quad m = 1, \dots, N, \quad (16)$$

or, equivalently,

$$\mathbf{Q}_m^{(l)} \boldsymbol{\Omega} = \mathbf{0}, \quad (17)$$

where $\mathbf{Q}_m^{(l)}$ is the $2N \times N_{\text{seg}}$ coefficient matrix and the stabilization order $l = 1, \dots, K_\tau$.

Given an optimal solution, one finds that the infidelity as a function of the motional-mode frequencies drift is different from the laser detuning in some parameter regimes. It results from the fast oscillatory terms of the spin-motion constraints. Therefore, it is necessary to stabilize against the laser detuning errors if one does not use the rotating wave approximation in spin-motion constraints. Specifically, one requires

$$\frac{\partial^p \alpha_j^m}{\partial \mu^p} = 0, \quad m = 1, \dots, N, \quad (18)$$

or

$$\mathbf{P}_m^{(p)} \boldsymbol{\Omega} = \mathbf{0}, \quad (19)$$

where $\mathbf{P}_m^{(p)}$ is the $2N \times N_{\text{seg}}$ coefficient matrix and the stabilization order $p = 1, \dots, K_\mu$.

Since the robust constraints are linear in $\boldsymbol{\Omega}$, we can expand the matrix \mathbf{M} to include these constraints under the consideration of robustness. More importantly, we can also improve robustness against the mixed drifts through including the corresponding constraints simultaneously. The explicit expressions of $\mathbf{K}_m^{(k)}$, $\mathbf{Q}_m^{(l)}$, and $\mathbf{P}_m^{(p)}$ are given in Appendix B.

C. Optimization schemes

From the discussions in the previous subsections, there are $2N(1 + K_\omega + K_\tau + K_\mu)$ homogeneous linear equations if one considers robustness against aforementioned parameter drifts to a desired order. We use the singular value decomposition to solve these linear equations and the solution space we are concerned about is the right singular vectors. When N_{seg} is larger than the number of linear constraints, there exist at least $N_0 = N_{\text{seg}} - 2N(1 + K_\omega + K_\tau + K_\mu)$ nontrivial solutions, also known as the null space of \mathbf{M} .

We define the null space as an $N_{\text{seg}} \times N_0$ matrix $\boldsymbol{\Omega}_{\text{null}}$, whose columns $\boldsymbol{\Omega}_{\text{null}}^{[i]}$ form an orthogonal basis of the null space of \mathbf{M} , i.e.,

$$\mathbf{M}\boldsymbol{\Omega}_{\text{null}}^{[i]} = \mathbf{0}, \quad i = 1, \dots, N_0. \quad (20)$$

The arbitrary linear combination vector $\boldsymbol{\Omega}'_{\text{null}}$ in the null space satisfies the linear constraints and takes a certain value C , i.e.,

$$\boldsymbol{\Omega}_{\text{null}}'^T \mathbf{D} \boldsymbol{\Omega}'_{\text{null}} = C. \quad (21)$$

We can obtain a valid solution to achieve an ideal operation by a simple normalization of $\boldsymbol{\Omega}'_{\text{null}} \rightarrow \sqrt{\frac{\pi}{4|C|}} \boldsymbol{\Omega}'_{\text{null}}$. Therefore, we can perform the two-qubit quantum gate with an ideal fidelity for any given gate duration τ and detuning μ . However, as $\boldsymbol{\Omega}'_{\text{null}}$ is arbitrary, this method does not ensure that the solution is efficient and optimal.

We should remark that for realistic experimental parameters, the effective Rabi frequency cannot be too large, and an increasing power leads to a reduced gate fidelity. Additionally, since one applies discrete AM pulses that are equally segmented in time, a large relative change of amplitudes in

neighboring pulses is hard to be physically implemented, especially when one performs fast gates. Therefore, by using the N_0 degrees of freedom, we expect one can optimize with respect to certain experimentally favorable conditions, such as the laser power or the pulse gradient. For convenience, we refer to the laser power optimization scheme as scheme I, and the pulse gradient optimization scheme as scheme II.

The root-mean-square (rms) Rabi frequency power P in scheme I can be defined as

$$P^2 = \frac{1}{N_{\text{seg}}} \sum_{n=1}^{N_{\text{seg}}} \Omega_n^2 = \frac{1}{N_{\text{seg}}} \boldsymbol{\Omega}^T \mathbf{I} \boldsymbol{\Omega}, \quad (22)$$

where \mathbf{I} is the $N_{\text{seg}} \times N_{\text{seg}}$ identity matrix.

The rms Rabi frequency gradient G of scheme II can be expressed as

$$G^2 = \frac{1}{N_{\text{seg}} + 1} \sum_{n=0}^{N_{\text{seg}}} (\Omega_{n+1} - \Omega_n)^2 = \frac{1}{N_{\text{seg}} + 1} \boldsymbol{\Omega}^T \mathbf{T} \boldsymbol{\Omega}, \quad (23)$$

where \mathbf{T} is the $N_{\text{seg}} \times N_{\text{seg}}$ tridiagonal matrix with $T_{ij} = 2$ for $i = j$ and $T_{ij} = -1$ for $i = j \pm 1$, and $\Omega_0 = \Omega_{N_{\text{seg}}+1} = 0$.

Our goal now is to linearly combine the orthonormal null space vectors $\boldsymbol{\Omega}_{\text{null}}^{[i]}$ with real expansion amplitudes $\boldsymbol{\Lambda}$ to find the optimal solution vector in the null space:

$$\boldsymbol{\Omega}_{\text{opt}} = \sum_{i=1}^{N_0} \Lambda_i \boldsymbol{\Omega}_{\text{null}}^{[i]}. \quad (24)$$

We wish to minimize the laser amplitude, in other words, the rms Rabi frequency or the change of discrete pulse shape, i.e., the rms pulse gradient. By using the null space, the spin-motion decoupling constraints are satisfied exactly, and we can achieve the minimization under the accumulated phase quadratic constraint.

Now, one can formulate the constrained optimization problem as

$$\begin{aligned} f(\boldsymbol{\Lambda}) &= \min(\boldsymbol{\Lambda}^T \mathbf{H} \boldsymbol{\Lambda}), \\ \text{s.t. } |\boldsymbol{\Lambda}^T \mathbf{R} \boldsymbol{\Lambda}| &= \frac{\pi}{4}, \end{aligned} \quad (25)$$

where

$$\mathbf{H} = \begin{cases} \boldsymbol{\Omega}_{\text{null}}^T \mathbf{I} \boldsymbol{\Omega}_{\text{null}}, & \text{scheme I,} \\ \boldsymbol{\Omega}_{\text{null}}^T \mathbf{T} \boldsymbol{\Omega}_{\text{null}}, & \text{scheme II,} \end{cases} \quad (26)$$

$$\mathbf{R} = \boldsymbol{\Omega}_{\text{null}}^T \mathbf{D} \boldsymbol{\Omega}_{\text{null}}. \quad (27)$$

D. Hypersurface-tangent method for optimization

In this paper, we propose the geometrical tangent method of hypersurfaces to find the minimum of the objective function under the accumulated phase constraint. The symmetric matrix \mathbf{R} of $N_0 \times N_0$ can be spectrally decomposed as

$$\mathbf{R} = \sum_{k=1}^{N_0} a_k (\mathbf{A}^{(k)})^T \mathbf{A}^{(k)}, \quad (28)$$

where a_k is the k th eigenvalue of \mathbf{R} and $\mathbf{A}^{(k)}$ is the corresponding eigenvector. Expanding $\boldsymbol{\Lambda}$ into the eigenvectors of \mathbf{R} , one can linearly combine the vector of expansion amplitude $\boldsymbol{\Lambda}$ by

the set of vectors $\mathbf{A}^{(k)}$ according to

$$\boldsymbol{\Lambda} = \sum_{k=1}^{N_0} v_k \mathbf{A}^{(k)}. \quad (29)$$

The accumulated phase constraint can be then written as

$$\frac{\pi}{4} = |\boldsymbol{\Lambda}^T \mathbf{R} \boldsymbol{\Lambda}| = \left| \sum_{k=1}^{N_0} v_k^2 a_k \right|. \quad (30)$$

It is important to note that if \mathbf{R} is positive or negative definite, Eq. (30) stands for an N_0 -dimensional quadratic hypersurface with principal axes $|a_k|^{-1/2}$, which we refer to the hypersurface S_1 . If \mathbf{R} has both positive and negative eigenvalues, the equation describes an N_0 -dimensional hyperboloid with principal axes $|a_k|^{-1/2}$, which we refer to as the hypersurface S_2 . For the latter case, the accumulated phase can be either $+\pi/4$ or $-\pi/4$.

Similarly, one can also spectrally decompose \mathbf{H} according to

$$\mathbf{H} = \sum_{k=1}^{N_0} b_k (\mathbf{B}^{(k)})^T \mathbf{B}^{(k)}, \quad (31)$$

where b_k is the k th eigenvalue of \mathbf{H} and $\mathbf{B}^{(k)}$ is the corresponding eigenvector. In a similar way, one can linearly combine the vector of expansion amplitude $\boldsymbol{\Lambda}$ by the set of vectors $\mathbf{B}^{(k)}$ according to

$$\boldsymbol{\Lambda} = \sum_{k=1}^{N_0} v_k \mathbf{B}^{(k)}, \quad (32)$$

and then the objective function can be expressed as

$$f = \min(\boldsymbol{\Lambda}^T \mathbf{H} \boldsymbol{\Lambda}) = \min \left(\sum_{k=1}^{N_0} v_k^2 b_k \right). \quad (33)$$

According to Eqs. (22) and (23), \mathbf{H} is a positive-definite matrix. For scheme I, by substituting Eq. (29) into the objective function directly, Eq. (33) is an N_0 -dimensional hypersphere and the eigenvector corresponding to the largest $|a_k|$ will be the optimal solution. In other words, the hypersphere is inscribed in the hypersurface S_1 or S_2 and just touches the hypersurface along the principal axis with the smallest length.

For scheme II, Eq. (33) is also an N_0 -dimensional hypersurface with principal axes $|b_k|^{-1/2}$, which is also hypersurface S_1 . Thus, geometrically speaking, Eqs. (30) and (33) are N_0 -dimensional hypersurfaces with different principal axes at different coordinates. The point of tangency of the two hypersurfaces corresponds to the minimum of the objective function. If Eq. (30) is the hypersurface S_1 , the inscribed cone is the minimization of the objective function and the circumscribed cone is the maximum value. The accumulated phase is $\pi/4$ ($-\pi/4$) for positive (negative) definite matrix \mathbf{R} . On the other hand, for the hypersurface S_2 of Eq. (30), due to the property of the indefinite matrix, the accumulated phase can be $\pm\pi/4$ and then there exist two inscribed cones. One can obtain the minimum of the objective function by comparing the points of tangency of the different accumulated phase value.

Computationally, we get the optimal solution \mathbf{A}_{opt} and the minimum of the objective function f_{min} by solving the following equations. First, we transform the coordinates of the vectors \mathbf{A}_{all} to the new coordinates \mathbf{B}_{all} by making use of the transformation matrix \mathbf{T} :

$$\mathbf{B}_{\text{all}} = \mathbf{T}\mathbf{A}_{\text{all}}. \quad (34)$$

Note that $\mathbf{A}^{(k)}$ and $\mathbf{B}^{(k)}$ are the k th row vectors of \mathbf{A}_{all} and \mathbf{B}_{all} respectively. Using the transformation matrix, we can now obtain

$$f = \min(\mathbf{v}^T \boldsymbol{\Sigma} \mathbf{v}) = \min[\mathbf{v}^T (\mathbf{T}^T \boldsymbol{\Sigma} \mathbf{T}) \mathbf{v}], \quad (35)$$

$$|\mathbf{v}^T \mathbf{O} \mathbf{v}| = \pi/4, \quad (36)$$

where $\boldsymbol{\Sigma}$ is a diagonal matrix with element b_k , \mathbf{O} is a diagonal matrix with element a_k , \mathbf{v} is the column vector with element v_k , and \mathbf{v} is the column vector with element v_k .

The point of tangency is obtained by solving the following equation:

$$\mathbf{v}^T \boldsymbol{\Pi} \mathbf{v} = 0, \quad (37)$$

in which

$$\boldsymbol{\Pi} = (\mathbf{O}' - \mathbf{T}^T \boldsymbol{\Sigma}' \mathbf{T}), \quad (38)$$

where $\boldsymbol{\Sigma}'$ is a diagonal matrix with element b_k/f , and \mathbf{O}' is a diagonal matrix with element $4a_k/\pi$ for the positive-definite case, $-4a_k/\pi$ for the negative-definite case, or $\pm 4a_k/\pi$ for an indefinite matrix.

The minimum objective function f_{min} , i.e., the point of the inscribed tangent, corresponds to the maximum eigenvalue of $\boldsymbol{\Pi} = (\mathbf{O}' - \mathbf{T}^T \boldsymbol{\Sigma}' \mathbf{T})$ equal to zero, and the corresponding eigenvector of $\boldsymbol{\Pi}$ is the optimized vector. When the eigenvalues of $\boldsymbol{\Pi}$ are all negative, it means that there is no point of intersection of these two hypersurfaces. We can successfully find the satisfactory gate solution \mathbf{v} by a root finding method. The choice of initial guess of the root finding method is not sensitive in search of the solution due to the monotonicity of the maximum eigenvalue of $\boldsymbol{\Pi}$ with the minimum objective function f_{min} . To reduce the number of iterations, we take the minimum of b_k as the initial guess, in which case the principal axis with the longest length of the hypersurface is intersectant with the hypersurface S_1 or S_2 .

In this way, our optimization problem is solved:

$$\mathbf{A}_{\text{opt}} = \sum_{k=1}^{N_0} v_k \mathbf{A}^{(k)}, \quad (39)$$

$$\boldsymbol{\Omega}_{\text{opt}} = \sum_{i=1}^{N_0} \Lambda_{\text{opt}}^{[i]} \boldsymbol{\Omega}_{\text{null}}^{[i]}. \quad (40)$$

We want to point out that, in the discussion above, we require that the pulse segments be larger than the number of constraints, in which case the method allows N_0 null space vectors $\boldsymbol{\Omega}_{\text{null}}^{[i]}$ of \mathbf{M} with singular values $\lambda_i = 0$, $i = 1, \dots, N_0$. In this method, we can achieve an ideal fidelity for any τ and μ without parameters scanning and can efficiently optimize the laser power or the pulse gradient. Therefore, we refer this method to the exact AM method.

E. Approximated null space method for a few segments

When the pulse segments are fewer than the number of linear constraints, there does not exist $\boldsymbol{\Omega}_{\text{null}}$ which exactly satisfies Eq. (12). However, in the current experimental conditions, one can also use a few segments to achieve a high-fidelity quantum gate by scanning the gate parameters such as the gate duration [29–32,43,44,53]. The exact method for a few segments is the highest-fidelity solution. Due to the fact that most of the motional modes have relatively low populations and do not need to be perfectly decoupled, we can construct an approximated null space as the optimized solution space at the cost of a negligible amount of fidelity.

Through the singular value decomposition of \mathbf{M} , we obtain its singular values $\lambda_1, \lambda_2, \dots, \lambda_{N_{\text{seg}}}$, ordered according to their absolute values:

$$0 \leq |\lambda_1| \leq |\lambda_2| \leq \dots \leq |\lambda_{N_{\text{seg}}}|. \quad (41)$$

We notice that a few singular values are particularly small in magnitude and the corresponding singular vectors with a suitable normalization can obviously decrease the laser power or reduce the pulse gradient. Considering the above observation, we can therefore effectively relax the spin-motion decoupling constraints into

$$\mathbf{M}\boldsymbol{\Omega} \approx \mathbf{0}. \quad (42)$$

In this way, we can construct an approximated null space at the cost of a negligible amount of fidelity by including L_{cut} singular vectors whose singular values are very close to zero, which is similar to the treatment in Ref. [46]. We adjust the value of L_{cut} according to the fulfillment of $\delta\bar{F} < \delta F_t$, where δF_t is the threshold of fidelity which is acceptable in the current experiments. We refer to this method as the ANS method, which yields pulses with lower laser power or pulse gradient than the highest-fidelity solution. Please note that this method is also valid for many pulse segments if one extends the null space by including singular vectors corresponding to L_{cut} nonzero singular values. The dimension of the extended null space (ENS) is $N'_0 = N_0 + L_{\text{cut}}$. For the latter case of many segments, we call it the ENS method.

IV. NUMERICAL RESULTS

In this section, we will present our main results based on our numerical schemes for optimizing a robust two-qubit quantum gate in a linear chain of $^{171}\text{Yb}^+$ ions. For realistic parameters, we consider a chain of 20 ions in a hybrid trap potential which is specified by $\gamma_4 = 0.5333$ and choose the transverse trapping frequency $\omega_x = \omega_y = 2\pi \times 3$ MHz and the axial trapping frequency $\omega_z = 2\pi \times 0.05$ MHz. As a result, the 20 ions will have a nearly uniform spacing with a relative standard deviation (RSD) of 5.63%. The temperature is set to $k_B T = \hbar\omega_x$ to give an average phonon number of $\bar{n}_m \approx 0.5$ for each transverse mode, which can be easily achieved with the Raman sideband cooling.

To implement a phase-insensitive two-qubit $\sigma_{\phi_s} \sigma_{\phi_s}$ gate, two counterpropagating laser beams with equal but opposite detuning are shined on the ions along the $\pm x$ directions. For the $^{171}\text{Yb}^+$ qubit transitions, the laser beams have wavelengths around $\lambda = 355$ nm. Throughout this paper, we set

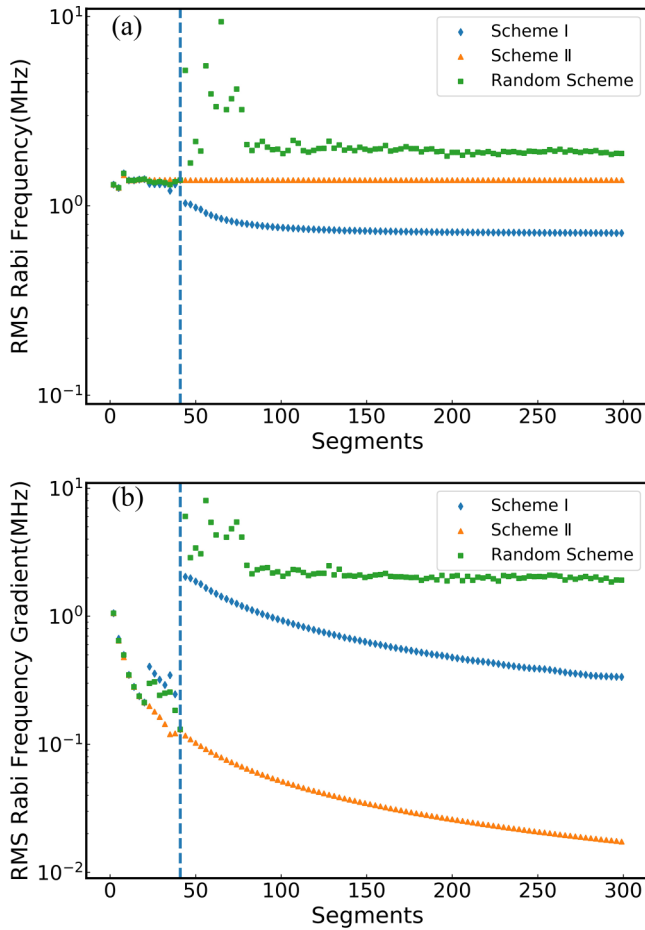


FIG. 1. Comparisons of three different optimization schemes: scheme I (the blue thin diamonds), scheme II (the orange triangles), and the random scheme (the green squares). The rms Rabi frequency in (a) and the rms Rabi frequency gradient of pulse shape in (b) are shown as a function of the pulse segments N_{seg} on qubits (9, 11) for the gate duration $\tau = 280 \mu\text{s}$ and the laser detuning $\mu = 0.978\omega_x$. The vertical blue dashed line at $N_{\text{seg}} = 41$ (i.e., the number of constraints) is drawn to distinguish the ANS method and the exact method for different pulse segments.

the infidelity threshold to $\delta F_t = 10^{-4}$, which is acceptable in experiments after accounting for intensity fluctuations, the motional-mode heating, the motional dephasing, the laser dephasing, the off-resonant photon scattering, etc. The infidelity threshold roughly corresponds to the spontaneous scattering limit.

A. Comparison of the optimization schemes

Considering the experimental feasibility in realizing the effective Rabi frequency and its requirement in minimizing the pulse gradient, we have proposed the geometrically hypersurface-tangent method to obtain the optimized efficient solution on the basis of high fidelity. Here, we want to check the effectiveness and performance of our method in finding the optimal solution for different numbers of pulse segments. For doing so, we vary the number of segments N_{seg} from several up to 300 for $\tau = 280 \mu\text{s}$ and $\mu = 0.978\omega_x$. In Fig. 1, we show the rms Rabi frequency and the rms Rabi frequency gradient

of optimization schemes. Note that, for a two-qubit nonrobust quantum gate in a chain of 20 ions, the number of constraints is 41. When the number of pulse segments is fewer than the number of constraints, we can apply the ANS method and set $\delta F_t = 10^{-4}$ to construct an optimal solution space. For the number of pulse segments $N_{\text{seg}} \geq 41$, we apply the exact method in which the quantum gate can be regarded as an ideal operation.

To validate our scheme for the optimal solution, we randomly select the normalized vector as the solution vector and adjust the Rabi frequency to satisfy the remaining accumulated phase condition. For a fair comparison, we repeat this process six times and average the results. We call this scheme the random scheme. As shown in Fig. 1, we compare the results of the rms Rabi frequency of scheme I (laser power optimization), scheme II (pulse gradient optimization), and the random scheme.

One finds that scheme I is obviously efficient for any pulse segments, especially for pulse segments $N_{\text{seg}} \geq 41$ in Fig. 1(a). Similarly, the rms pulse gradient of scheme II in Fig. 1(b) is considerably lower than the other two methods, particularly effective for $N_{\text{seg}} \geq 41$. For example, the rms Rabi frequency gradient of $N_{\text{seg}} = 300$ has been reduced to 0.85% compared with that of the random scheme and 5.17% compared with that from scheme I.

In addition, we find that the optimization of scheme II is more obvious compared with scheme I. One can indeed reduce the gradient of the pulse effectively by using scheme II, where only a slight increase of the laser power is needed. This advantage of the gradient optimization in scheme II is readily valid in many parameters regions when the laser detuning is around the range of motional-mode frequencies.

Finally, in order to demonstrate the optimized effective Rabi frequency Ω , we choose to show the results for two cases $N_{\text{seg}} = 35$ and 120 in Appendix C. From comparisons of all the three schemes for the specific examples, we conclude that our optimization schemes for the laser power and the gradient of the pulse are indeed effective.

B. Approximated and extended null space

In current experiments, the fidelity of a two-qubit AM gate in the trapped-ion quantum computation is around 98% [43,44,53], due to various sources of noise. Consequently, we can trade a negligible amount of gate fidelity for a more efficient solution, especially for the case of a few segments. From our discussions in previous sections, this can be accomplished by constructing an approximate null space of \mathbf{M} for a few pulse segments $N_{\text{seg}} < 2N + 1$ and an extended null space of \mathbf{M} for many pulse segments $N_{\text{seg}} \geq 2N + 1$. The solution space includes L_{cut} singular vectors with nonzero singular values, as long as $\delta \bar{F} < \delta F_t$, where $\delta \bar{F} = 1 - \bar{F}$ is the quantum gate infidelity and δF_t is the threshold infidelity of the gate.

As an example, we present results of the ANS method for $N_{\text{seg}} = 35$. Again, we keep the gate duration and the detuning fixed, i.e., $\tau = 200 \mu\text{s}$ and $\mu = 0.978\omega_x$. As a function of L_{cut} , we show the infidelity $\delta \bar{F}$ versus the rms Rabi frequency and versus the Rabi frequency gradient in Figs. 2(a) and 2(b), respectively.

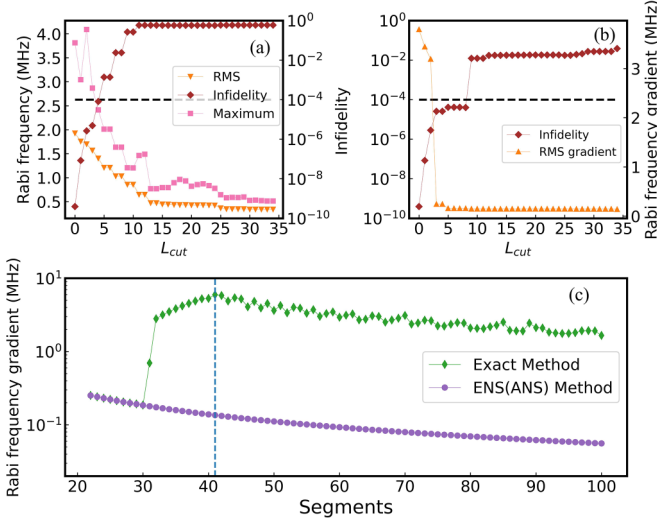


FIG. 2. Performance of the approximated (extended) null space method. For the gate duration $\tau = 200 \mu\text{s}$, the detuning $\mu = 0.978\omega_x$, and the number of pulse segments $N_{\text{seg}} = 35$, we show (a) infidelity $\delta\bar{F}$, the corresponding rms, and maximum Rabi frequency as a function of L_{cut} for scheme I and (b) infidelity $\delta\bar{F}$ and the corresponding rms Rabi frequency gradient as a function of L_{cut} for scheme II. In both (a) and (b), a horizontal dashed line at $\delta\bar{F} = 10^{-4}$ (an acceptable infidelity for current experiments) is drawn to guide the eye. In (c), the rms Rabi frequency gradient of scheme II as a function of the pulse segments N_{seg} is compared for the exact method against the ANS (or ENS) method, where a vertical dashed line marks the number of constraints 41.

As can be seen, the infidelity increases with the increase of L_{cut} , reaching 10^{-4} at $L_{\text{cut}} = 5$ in which case the rms Rabi frequency can be dropped by 30% compared with that of $L_{\text{cut}} = 0$ in Fig. 2(a). Additionally, the maximum Rabi frequency drops in accordance with the optimized rms Rabi frequency. The result of saving with L_{cut} is more obvious for scheme II, as shown in Fig. 2(b). For $L_{\text{cut}} = 8$, the rms Rabi frequency gradient has been reduced to 4% of that for $L_{\text{cut}} = 0$. This shows a large number of singular vectors of \mathbf{M} may indeed be used as the variational space to optimize the solution at only a negligible fidelity cost.

In Fig. 2(c), we compare the rms Rabi frequency gradient of the exact method with that of the ENS (ANS) method as a function of the pulse segments N_{seg} . As can be seen in Fig. 2(c), the ENS (ANS) method provides a pulse shape smooth advantage for $N_{\text{seg}} > 30$. It is noteworthy that the ANS method has coincided with the exact method for $N_{\text{seg}} < 30$. The reason is simple: the infidelity of the pulse for $N_{\text{seg}} < 30$ is higher than 10^{-5} , and then there exist very few singular vectors with nonzero singular values to guarantee $\delta\bar{F} < \delta F_t$.

Finally, we wish to compare the laser power as a function of the gate duration τ in scheme I. In Fig. 3, we present the laser power of the exact method with the ENS method for $K_\omega = 0$ and 1. Over a large range of gate duration, the ENS method offers significant power savings at the cost of a negligible fidelity. The power requirement dramatically increases as the gate duration is shortened because of the high excitation

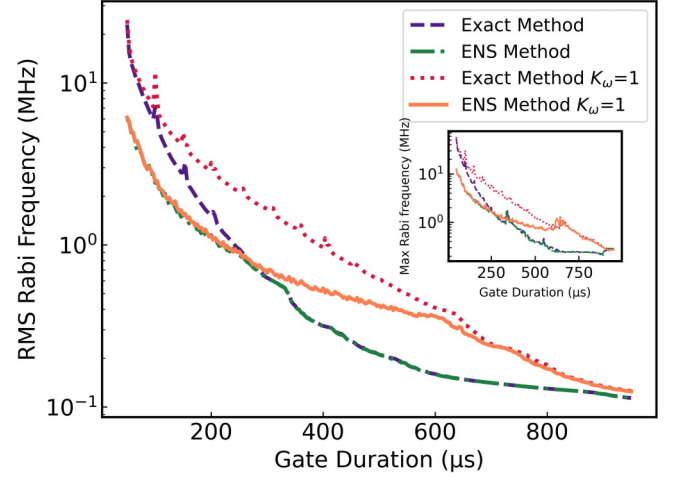


FIG. 3. Comparisons of the rms Rabi frequency as a function of the gate duration τ from the exact method and from the ENS method in scheme I for $K_\omega = 0$ and 1, $\mu = 0.978\omega_x$, and $N_{\text{seg}} = 300$, which are represented by different line styles. Also shown in the inset is the corresponding maximum Rabi frequency.

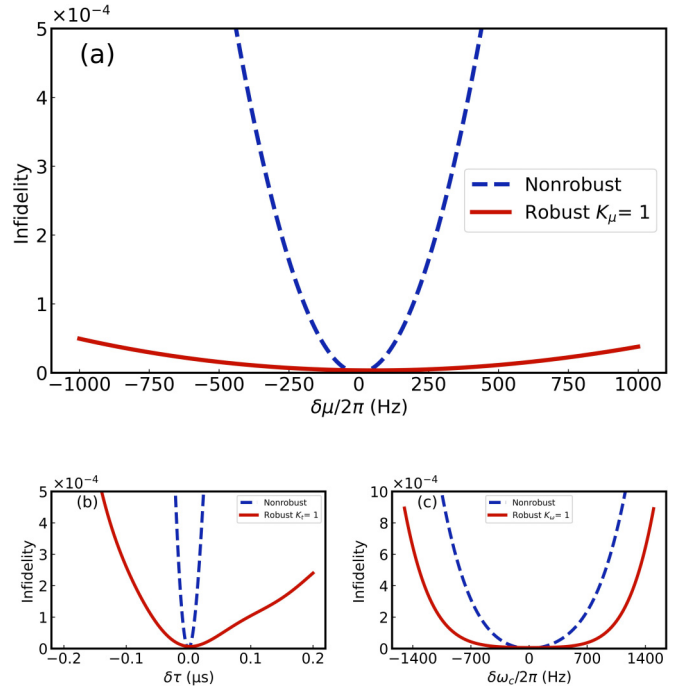


FIG. 4. Comparisons of infidelity $\delta\bar{F}_a$ as a function of the parameter drift for the two-qubit gate with robust order 1 and the nonrobust gate. For the pulse segments $N_{\text{seg}} = 32$ and the detuning $\mu = 0.978\omega_x$, results are shown for (a) the laser detuning drift for $\delta\mu = (-2\pi \times 1000, 2\pi \times 1000)$ Hz and the gate duration $\tau = 150 \mu\text{s}$, (b) the gate duration drift for $\delta\tau = (-0.2, 0.2) \mu\text{s}$ and the gate duration $\tau = 150 \mu\text{s}$, and (c) the motional-mode frequencies random static drift for $\delta\omega_c = (-2\pi \times 1500, 2\pi \times 1500)$ Hz and the gate duration $\tau = 280 \mu\text{s}$. In the above figures, the red solid line and the dark blue dashed line represent the infidelity $\delta\bar{F}_a$ of the two-qubit gate with robust order 1 and the nonrobust gate.

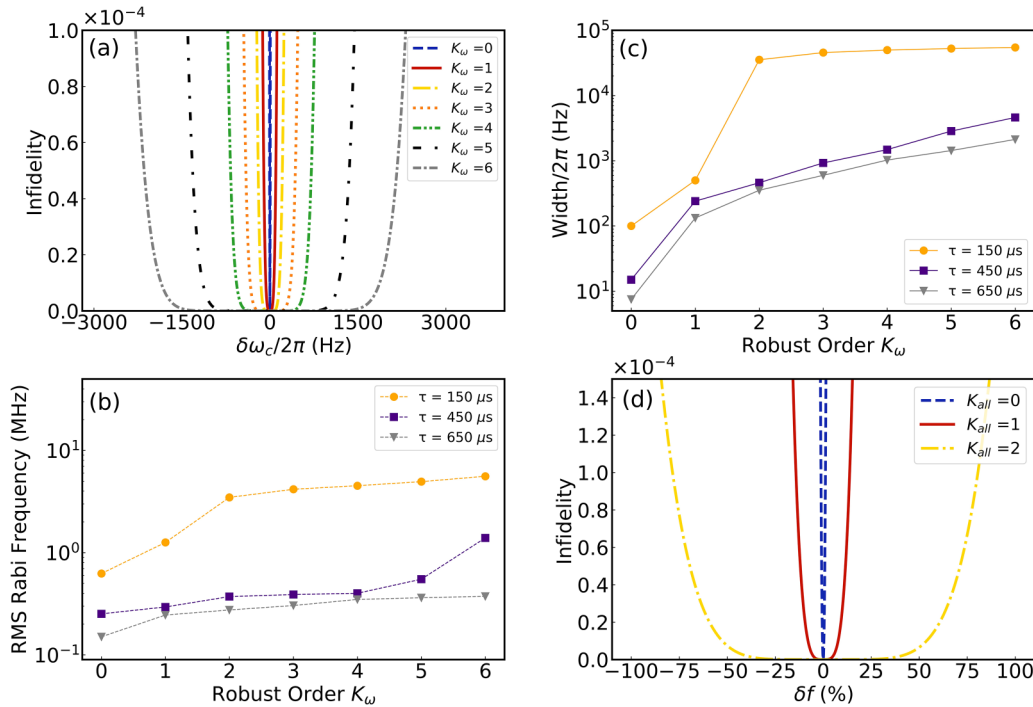


FIG. 5. Robust results of the exact method with the laser power optimization for the detuning $\mu = 0.995\omega_x$ and the pulse segments $N_{\text{seg}} = 358$. (a) The infidelity $\delta\bar{F}_a$ of stabilized pulses $K_\omega = 0, 1, \dots, 6$ as a function of the motional mode frequencies random drifts for the pulse duration $\tau = 450 \mu\text{s}$. (b) The width of infidelity curves extracted at tolerance $\epsilon = 10^{-4}$ for different durations of pulse, as a function of the robust order K_ω . (c) The rms power requirement of different durations of pulse, as a function of the robust order K_ω . (d) The infidelity $\delta\bar{F}_a$ of stabilized pulses $K_{\text{all}} = 0, 1, 2$ as a function of simultaneous drifts with different signs of all parameters with the gate duration drift range $\delta\tau = (-0.112, 0.112) \mu\text{s}$, the detuning drift range $\delta\mu = (2\pi \times 430, -2\pi \times 430) \text{ Hz}$, and the random motional-mode frequencies drift range $\delta\omega_c = (-2\pi \times 550, 2\pi \times 550) \text{ Hz}$, in which the horizontal axis δf represents the percentage change of the above parameters.

of the motional modes, as shown in Fig. 3. Of course, the power requirement of the robust quantum gate $K_\omega = 1$ is higher than that of the nonrobust gate because of increased constraints. To clearly verify that the rms optimization is effective to the maximum Rabi frequency, we plot the maximum Rabi frequency as the function of gate duration τ in the inset of Fig. 3. As can be seen, the average power minimization is essentially as good as that of the maximum Rabi frequency of the pulse.

C. Robust gates

Aforementioned, in the present paper, we present a unified linear framework to suppress the dominant sources of the infidelity of entangling gates, which is related to the spin-motion residual coupling. In Fig. 4, we compare the results for robust order 1 with the nonrobust pulse against possible errors, including motional frequencies, the detuning, and the gate duration. In this case, we use the approximate infidelity $\delta\bar{F}_a$ which is given by Eq. (11). We present the laser power optimization results of a few segments for $N_{\text{seg}} = 32$ and $\mu = 0.978\omega_x$. As we can see in Fig. 4(a), the robust pulse can tolerate detuning errors dramatically more than the nonrobust case. The infidelity curve of $K_\mu = 1$ is still lower than 10^{-4} when $\delta\mu = 2\pi \times 1000 \text{ Hz}$.

For the robustness against motional frequencies drift, we investigate the case of the random static drifts, which is closer to the experimental drifts. We choose N random numbers g

from a Gaussian distribution with zero mean and standard deviation $\sigma = 1$. Thus, all modes frequencies drift randomly according to ω to $\omega + \delta\omega_c g$, where $\delta\omega_c$ is the scaling factor and ω is all motional-mode frequencies. Again, we repeat the random process six times and average for the infidelity. As shown in Fig. 4(c), the result for the motional frequencies robustness is as good as those in Figs. 4(a) and 4(b). For a few segments, our results show that the robust method significantly improves fidelity even for robust order 1.

In order to investigate the effect of the high-order robustness, we choose another trap potential with $\gamma_4 = 5$, in which case the high-order parameters drift has great influence on the fidelity, and discuss the situation of many pulse segments. In Fig. 5(a), the infidelity of robust pulses $K_\omega = 0, 1, \dots, 6$ is shown as a function of the extent of the mode frequencies random drifts. We have defined the drift width of the infidelity curves, extracted at error tolerance $\epsilon = 10^{-4}$ to describe the robustness. Intuitively, the width $\delta\omega_c$ increases from $2\pi \times 15$ to $2\pi \times 4605 \text{ Hz}$ as K_ω is increased from 0 to 6 in Figs. 5(a) and 5(b).

In Fig. 5(b), we find that the width $\delta\omega_c$ increases with the order K_ω and the faster gate has a significantly better performance. The effect of the robustness increases inversely with the gate duration. The power requirement of the stabilized pulses for each K_ω of different gate duration is shown in Fig. 5(c). Obviously, when more constraint conditions are added, the size of the null space contracts and leads to an

increase in the laser power. In Fig. 5(d), we present the robustness of the simultaneous drifts with the gate duration, the motional-mode frequencies, and the laser detuning with different signs of the drift direction. As observed, these results confirm that the robust method can improve the fidelity significantly even for simultaneous experimental drifts.

D. Scaling to a larger number of ions

Scalability is one of the challenging issues in the trapped-ion quantum computation. One promising proposal is to use an architecture called the quantum charge-coupled device where the entanglement is first generated in individual zones and then distributed to other regions by the classical ion shuttling technique. However, the fidelity of multiqubit gates is significantly degraded for higher-temperature ion chains because of the ions' transport and this technique demands extremely exquisite control of ion positions. Another method to distribute quantum information between modules utilizes photons to entangle ions located in separate regions. This method is often referred to as remote entanglement photonic interconnects and is limited by the photon collection efficiency.

Therefore, it is essential and meaningful to perform high-fidelity, high-speed robust operations in a long linear chain. In this subsection, to test the scalability of our optimization schemes, we generalize our ANS method to a longer ion chain in a hybrid potential and investigate the effectiveness of the optimization. To verify its effectiveness, we compare the exact method and the ANS method of scheme I with $\tau = 200 \mu\text{s}$, $\mu = 0.5(\omega_{\max} + \omega_{\min})$, and the pulse segments $N_{\text{seg}} = 2N$. The results are presented in Fig. 6. As we can see, the ANS method is still always effective with the increase of the number of ions while the rms Rabi frequency of the exact method increases greatly with the number of ions. In fact, the ANS method of scheme II (the gradient optimization) works

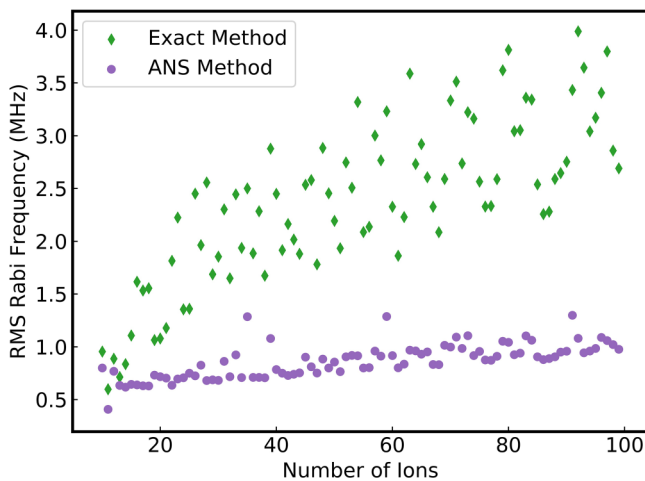


FIG. 6. rms Rabi frequency from the exact method (the green diamonds) and the ANS method (the purple circles) as a function of the number of ions with the gate duration $\tau = 200 \mu\text{s}$, the pulse segments $N_{\text{seg}} = 2N$, and the detuning $\mu = 0.5(\omega_{\max} + \omega_{\min})$, where ω_{\max} and ω_{\min} are the maximum and the minimum of the motional frequencies, respectively.

equally well with the increase of the ion number, whose results are not shown but similar to the laser power optimization.

V. CONCLUSIONS

In this paper, we focus on the segmented amplitude modulation technique and propose a geometrically hypersurface-tangent method to perform robust, high-fidelity quantum gates with the least amount of laser power and the best smooth pulse shape favorable for experiments. For a few segments pulse, we have shown that one can apply the tradeoff method by constructing an approximated null space to improve the performance of gates. In addition, we improve the robustness of quantum gates against random drifts of motional frequencies, the gate duration drifts, the laser detuning drifts, and their combinations. Our numerical method is linear and extensible, which can provide scaling benefits in large systems. Our method demonstrates decisive advantages in improving the optimization of the stability, and will thus be useful for near-term quantum computation.

ACKNOWLEDGMENT

This work is supported by National Natural Science Foundation of China Grants No. 12234002 and No. 92250303.

APPENDIX A: EQUILIBRIUM POSITIONS AND MOTIONAL MODES

In this part, we present a brief introduction of the static equilibrium and motional mode spectrum of a one-dimensional (1D) ion chain in a Paul trap. In a typical linear Paul trap, the tight radial confinement is realized by using a combination of dc and rf fields, whereas the weak axial confinement is achieved by dc electrodes [49]. If the radial potential is sufficiently strong compared to the axial potential, the equilibrium configuration of ions must be along the axial direction. The equilibrium positions are determined by a balance between the axial confining fields and the mutual Coulomb repulsion. A uniform configuration can prevent the ions in the center coming too close, thus reducing the possible crosstalk in the ion state detection and enabling a high-fidelity manipulation with focused laser beams. To achieve a uniform configuration of a long linear chain, ion distributions in different axial potentials have been studied previously [31,47,48].

The authors of Ref. [47] showed that a purely quartic potential leads to a much more uniform ion chain compared to a quadratic potential at the center, but the distribution of the ions changes quickly at both edges. Additionally, the combination of the quadratic and quartic potentials has been proposed as the trapping potential [48]. Such a combination of potential can accommodate more ions uniformly distributed than the quadratic potential or the quartic potential only, avoiding zigzag transitions at the center of the chain.

We briefly present the results for a linear ion chain in a hybrid potential, consisting of a quadratic and a quartic potential with a dimensionless ratio. The formulation also holds for a quadratic or a quartic potential alone. For typical experimental parameters, the micromotion is small and

can be neglected for a 1D ion chain in a linear Paul trap. We calculate the equilibrium configuration as well as the collective motional modes by effectively treating the trap potential as a static pseudopotential, following the derivation in Refs. [48–50].

The potential energy of the ion chain in a hybrid axial potential is given by the following expression:

$$U = \sum_{i=1}^N \left(-\frac{1}{2} \alpha_2 z_i^2 + \frac{1}{4} \alpha_4 z_i^4 \right) + \sum_{i<j} \left(\frac{q^2}{4\pi \epsilon_0 |z_i - z_j|} \right), \quad (\text{A1})$$

where q is the charge of an ion, z_i is the axial position of the i th ion, N is the number of ions, ϵ_0 is the permittivity of free space, and α_2 and α_4 are the coefficients of the quadratic term and quartic term ($\alpha_2, \alpha_4 > 0$). For convenience, we rescale the positions z_i using a length scale $l_0^3 = q^2/4\pi \epsilon_0 \alpha_2$ and then $u_i = z_i/l_0$. Thus, the rescaled axial potential energy can be rewritten as

$$V = \sum_{i=1}^N \left(-\frac{1}{2} u_i^2 + \frac{1}{4} \gamma_4 u_i^4 \right) + \sum_{i<j} \frac{1}{|u_i - u_j|}, \quad (\text{A2})$$

where $\gamma_4 = \alpha_4 l_0^2 / \alpha_2$ is a dimensionless ratio to characterize the strength of the quadratic potential relative to the quartic potential, which determines the equilibrium configuration.

For the hybrid potential, in order to homogenize the distribution of the ions, we introduce the RSD:

$$\text{RSD} = \frac{1}{\Delta z_i} \sqrt{\sum_{i=2}^N (\Delta z_i - \overline{\Delta z})^2 / (N-1)}, \quad (\text{A3})$$

where Δz_i is the distance between the two adjacent ($i-1$)th and i th ions in the chain and $\overline{\Delta z}$ denotes its average. So one can optimize the dimensionless ratio γ_4 to minimize the relative standard deviation.

We can get the equilibrium position u_i of the ions by solving the set of equations, $\frac{\partial V}{\partial u_i} = 0$, i.e., the minimization of the axial potential energy. For a given number of ions N and γ_4 , we can minimize the potential energy by using the Newton conjugate gradient algorithm or find the zero point of the gradient of the potential energy using a root-finding algorithm. The gradient and Hessian matrix elements of the axial potential energy can be respectively shown to be

$$\frac{\partial V}{\partial u_i} = -u_i + \gamma_4 u_i^3 - \sum_{i \neq j} \frac{u_i - u_j}{|u_i - u_j|^3} \quad (\text{A4})$$

and

$$\begin{aligned} \frac{\partial^2 V}{\partial u_i^2} &= -1 + 3\gamma_4 u_i^2 + \sum_{i \neq j} \frac{2}{|u_i - u_j|^3}, \\ \frac{\partial^2 V}{\partial u_i \partial u_j} &= \frac{2}{|u_i - u_j|^3}, \quad i \neq j. \end{aligned} \quad (\text{A5})$$

For the case of 20 ions considered in the main text, we compare the equilibrium positions for different types of potentials. As can be seen from Fig. 7, the ions in the hybrid potential are indeed much more evenly distributed across the chain compared to the quadratic or quartic potential only. In particular, $\gamma_4 = 0.5333$ is found to give a minimal RSD of

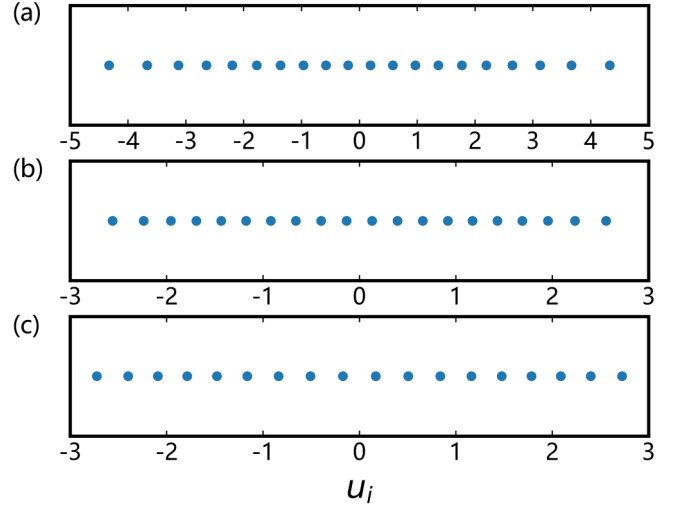


FIG. 7. Equilibrium configuration of 20 ions in different potentials: (a) a quadratic potential, (b) a quartic potential, and (c) a hybrid potential with $\gamma_4 = 0.5333$. Note that the ions in the hybrid potential are more uniform.

only 5.63% in the hybrid potential; in comparison, a quadratic potential gives rise to a RSD of 18.58% and a quartic potential gives rise to a RSD of 7.22%.

After finding the equilibrium positions $z_i^{(0)}$ along the axial direction, the complete expression of the potential energy can be written as

$$U_{\text{all}} = \sum_{i=1}^N \left(-\frac{1}{2} \alpha_2 z_i^2 + \frac{1}{4} \alpha_4 z_i^4 + \frac{1}{2} m_{\text{ion}} \omega_x^2 x_i^2 + \frac{1}{2} m_{\text{ion}} \omega_y^2 y_i^2 \right) + \sum_{i<j} \frac{q^2}{4\pi \epsilon_0 |\mathbf{r}_i - \mathbf{r}_j|}, \quad (\text{A6})$$

where $x_i^{(0)} = y_i^{(0)} = 0$, $z_i^{(0)} = l_0 u_i^{(0)}$, m_{ion} is the mass of the ion, and ω_x and ω_y are the radial trap frequencies. We can approximate the potential with its Taylor expansion around the equilibrium positions up to the second order. The dynamics of the system are described by the Lagrangian

$$L = \frac{1}{2} m \sum_{i=1}^N (\dot{q}_i)^2 - \frac{1}{2} m \sum_{i,j=1}^N A_{ij} q_i q_j, \quad (\text{A7})$$

where q_i is the displacement of the i th ion from the equilibrium position. The motional modes and their corresponding mode frequencies can be obtained through diagonalization of the symmetric Hessian matrix A_{ij} of the potential energy.

Using Eq. (A6), one can obtain the analytical expression $A_{ij}^{(x)}$ for the transverse motion

$$\left. \frac{\partial^2 U}{\partial x_i^2} \right|_{\mathbf{r}=\mathbf{r}^{(0)}} = \omega_x^2 - \sum_{i \neq j} \frac{\alpha_2}{m |u_{ij}|^3}, \quad (\text{A8})$$

$$\left. \frac{\partial^2 U}{\partial x_i \partial x_j} \right|_{\mathbf{r}=\mathbf{r}^{(0)}} = \frac{\alpha_2}{m |u_{ij}|^3}, \quad i \neq j \quad (\text{A9})$$

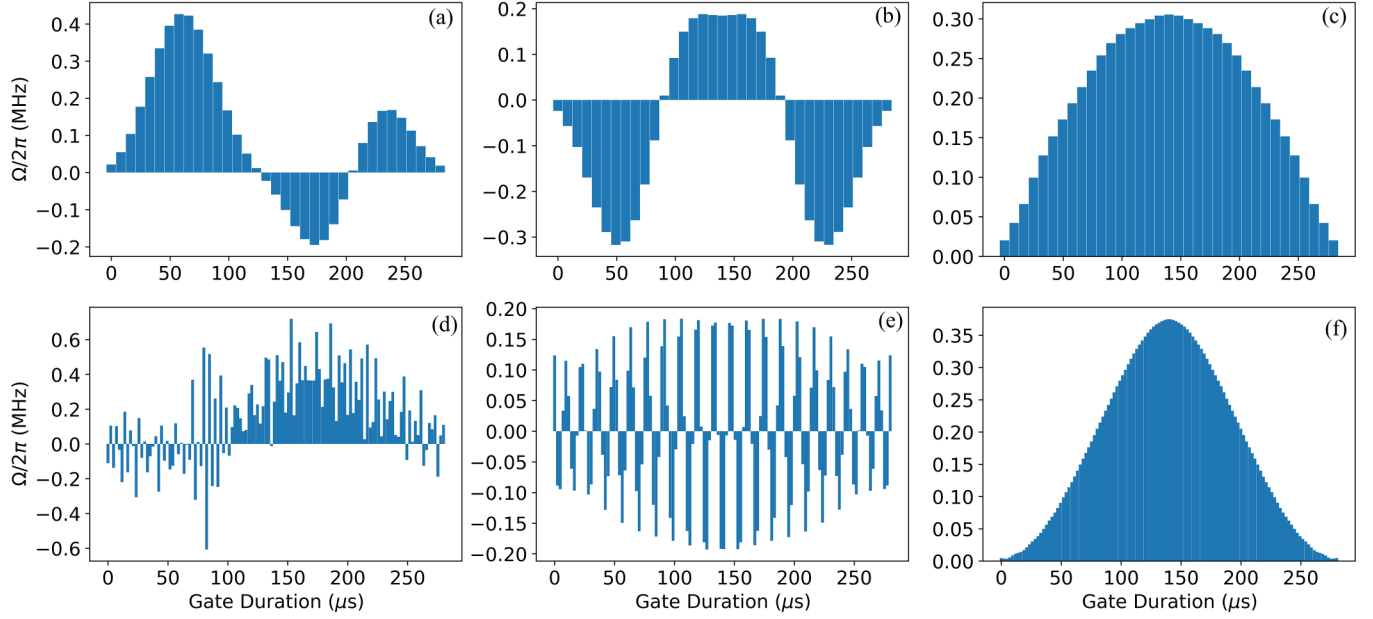


FIG. 8. The amplitude-modulated pulse sequences Ω of the driving field for an AM entangling gate for the ion pair (9, 11) in a 20-ion chain. (a)–(c) Comparisons of 35-segment pulses with infidelity $\delta F_i = 10^{-4}$ among the random scheme, scheme I, and scheme II using the approximated null space. (d)–(f) Comparisons of 120-segment pulses with infidelity $\delta \bar{F} = 0$ among the random scheme, scheme I, and scheme II using the exact null space.

and $A_{ij}^{(z)}$ for the axial motion

$$\left. \frac{\partial^2 U}{\partial z_i^2} \right|_{\mathbf{r}=\mathbf{r}^{(0)}} = \frac{\alpha_2}{m} \left(-1 + 3\gamma_4 + 2 \sum_{i \neq j} \frac{1}{|u_{ij}|^3} \right), \quad (\text{A10})$$

$$\left. \frac{\partial^2 U}{\partial z_i \partial z_j} \right|_{\mathbf{r}=\mathbf{r}^{(0)}} = -2 \frac{\alpha_2}{m |u_{ij}|^3}, \quad i \neq j, \quad (\text{A11})$$

where $u_{ij} = u_i - u_j$. The eigenvectors b_j^m are defined by $\sum_{i=1}^N A_{ij} b_i^m = \omega_m^2 b_j^m$, where ω_m is the transverse motional mode frequency with $m = 1, \dots, N$ being the motional mode index. Each motional mode represents an individual harmonic oscillator that can be quantized to give the phonon Hamiltonian.

APPENDIX B: MATRIX EXPRESSIONS

In this part, we give the explicit expressions for different matrices defined in Sec. III B. First, the elements of matrix \mathbf{M} for the j th qubit are given by

$$M(m, n) = \eta_j^m \int_{(n-1)\tau/N_{\text{seg}}}^{n\tau/N_{\text{seg}}} \sin(\mu t) \sin(\omega_m t) dt, \\ M(m + N, n) = \eta_j^m \int_{(n-1)\tau/N_{\text{seg}}}^{n\tau/N_{\text{seg}}} \sin(\mu t) \cos(\omega_m t) dt, \quad (\text{B1})$$

where j is the label of the ion, and $M(m, n)$ and $M(m + N, n)$ are respectively the real and the imaginary part of the residual decoupling of the m th motional mode.

The entanglement matrix \mathbf{S} is a real $N_{\text{seg}} \times N_{\text{seg}}$ matrix whose (p, q) component is given by

$$\mathbf{S}(p, q) = \begin{cases} 2 \sum_m \eta_i^m \eta_j^m \int_{\frac{(p-1)\tau}{N_{\text{seg}}}}^{\frac{p\tau}{N_{\text{seg}}}} dt_1 \int_{\frac{(q-1)\tau}{N_{\text{seg}}}}^{\frac{q\tau}{N_{\text{seg}}}} dt_2 \\ \times \sin(\mu t_1) \sin(\mu t_2) \sin[\omega_m(t_1 - t_2)], & (p > q), \\ 2 \sum_m \eta_i^m \eta_j^m \int_{\frac{(p-1)\tau}{N_{\text{seg}}}}^{\frac{p\tau}{N_{\text{seg}}}} dt_1 \int_{\frac{(p-1)\tau}{N_{\text{seg}}}}^{t_1} dt_2 \\ \times \sin(\mu t_1) \sin(\mu t_2) \sin[\omega_m(t_1 - t_2)], & (p = q), \\ 0, & (p < q). \end{cases} \quad (\text{B2})$$

The robustness against random drifts of motional-mode frequencies $\mathbf{K}_m^{(k)}$ is the $2N \times N_{\text{seg}}$ coefficient matrix, which represents the stabilization of the m th motional mode of the j th ion against mode frequency drifts to arbitrary order k . The real part $K_m^{(k)}(m, n)$ and the imaginary part $K_m^{(k)}(m + N, n)$ of the residual decoupling of the m th motional mode are given by

$$K_m^{(k)}(m, n) = \eta_j^m \int_{(n-1)\tau/N_{\text{seg}}}^{n\tau/N_{\text{seg}}} (t)^k \sin(\mu t) \sin(\omega_m t) dt, \\ K_m^{(k)}(m + N, n) = \eta_j^m \int_{(n-1)\tau/N_{\text{seg}}}^{n\tau/N_{\text{seg}}} (t)^k \sin(\mu t) \cos(\omega_m t) dt, \quad (\text{B3})$$

respectively, where $k = 1, \dots, K_\omega$ is the order of stabilization.

Similarly, the robustness against the gate duration $\mathbf{Q}_m^{(l)}$ is a $2N \times N_{\text{seg}}$ coefficient matrix, which is given by

$$Q_m^{(k)} = \frac{\eta_{jm}}{2i} \frac{[i(\mu + \omega_m)t]^l e^{i(\mu + \omega_m)t} \Big|_{\frac{(n-1)\tau}{N_{\text{seg}}}}^{\frac{n\tau}{N_{\text{seg}}}}}{i(\mu + \omega_m)} \\ - \frac{[i(\omega_m - \mu)t]^l e^{i(\omega_m - \mu)t} \Big|_{\frac{(n-1)\tau}{N_{\text{seg}}}}^{\frac{n\tau}{N_{\text{seg}}}}}{i(\omega_m - \mu)}, \quad (\text{B4})$$

where $l = 1, \dots, K_\tau$ is the order of stabilization. $Q_m^{(k)}(m, n)$ is the real part of Eq. (B4) and $Q_m^{(k)}(m + N, n)$ is its imaginary part.

Finally, the robustness against the laser detuning $\mathbf{P}_m^{(p)}$ is also a $2N \times N_{\text{seg}}$ matrix, which is represented as

$$P_m^{(p)} = \begin{cases} \eta_j^m (-1)^{\frac{p}{2}} \int_{(n-1)\tau/N_{\text{seg}}}^{n\tau/N_{\text{seg}}} t^p \sin(\mu t) \exp(i\omega_m t) dt, & p = 2, 4, 6, \dots, \\ \eta_j^m (-1)^{\frac{p-1}{2}} \int_{(n-1)\tau/N_{\text{seg}}}^{n\tau/N_{\text{seg}}} t^p \sin(\mu t) \exp(i\omega_m t) dt, & p = 1, 3, 5, \dots, \end{cases} \quad (\text{B5})$$

where $p = 1, \dots, K_\mu$ is the order of stabilization. $P_m^{(p)}(m, n)$ is the real part of Eq. (B5) and $P_m^{(p)}(m + N, n)$ is its imaginary part. The integral is similar to the robust calculation of the motional frequencies.

APPENDIX C: OPTIMIZED PULSE

In this part, we present the optimized effective Rabi frequency solutions Ω , which are plotted in Fig. 8. Here, we show the optimal results of two different pulse segments $N_{\text{seg}} = 35$ and 120. We find that the change between the adjacent pulse segments becomes very smooth in Figs. 8(c) and 8(f) which is favorable for experiments. It is remarkable that the maximal Rabi frequency of scheme I is considerably low along with the decrease of rms Rabi frequency compared with the random scheme, as shown in Figs. 8(d) and 8(e).

-
- [1] H.-X. Yang, J.-Y. Ma, Y.-K. Wu, Y. Wang, M.-M. Cao, W.-X. Guo, Y.-Y. Huang, L. Feng, Z.-C. Zhou, and L.-M. Duan, *Nat. Phys.* **18**, 1058 (2022).
- [2] R. J. Niffenegger, J. Stuart, C. Sorace-Agaskar, D. Kharas, S. Bramhavar, C. D. Bruzewicz, W. Loh, R. T. Maxson, R. McConnell, D. Reens, G. N. West, J. M. Sage, and J. Chiaverini, *Nature (London)* **586**, 538 (2020).
- [3] K. K. Mehta, C. Zhang, M. Malinowski, T.-L. Nguyen, M. Stadler, and J. P. Home, *Nature (London)* **586**, 533 (2020).
- [4] J. M. Pino, J. M. Dreiling, C. Figgatt, J. P. Gaebler, S. A. Moses, M. S. Allman, C. H. Baldwin, M. Foss-Feig, D. Hayes, K. Mayer, C. Ryan-Anderson, and B. Neyenhuis, *Nature (London)* **592**, 209 (2021).
- [5] X. Gu, A. F. Kockum, A. Miranowicz, Y.-Xi Liu, and F. Nori, *Phys. Rep.* **718-719**, 1 (2017).
- [6] M. H. Devoret and R. J. Schoelkopf, *Science* **339**, 1169 (2013).
- [7] M. Gong, M.-C. Chen, Y. Zheng, S. Wang, C. Zha, H. Deng, Z. Yan, H. Rong, Y. Wu, S. Li, F. Chen, Y. Zhao, F. Liang, J. Lin, Y. Xu, C. Guo, L. Sun, A. D. Castellano, H. Wang, C. Peng *et al.*, *Phys. Rev. Lett.* **122**, 110501 (2019).
- [8] F. Arute, K. Arya, R. Babbush, D. Bacon, J. C. Bardin, R. Barends, R. Biswas, S. Boixo, F. G. S. L. Brandao, D. A. Buell, B. Burkett, Y. Chen, Z. Chen, B. Chiaro, R. Collins, W. Courtney, A. Dunsworth, E. Farhi, B. Foxen, A. Fowler *et al.*, *Nature (London)* **574**, 505 (2019).
- [9] Y. Wu, W.-S. Bao, S. Cao, F. Chen, M.-C. Chen, X. Chen, T.-H. Chung, H. Deng, Y. Du, D. Fan, M. Gong, C. Guo, C. Guo, S. Guo, L. Han, L. Hong, H.-L. Huang, Y.-H. Huo, L. Li, N. Li *et al.*, *Phys. Rev. Lett.* **127**, 180501 (2021).
- [10] H.-S. Zhong, H. Wang, Y.-H. Deng, M.-C. Chen, L.-C. Peng, Y.-H. Luo, J. Qin, D. Wu, X. Ding, Y. Hu, P. Hu, X.-Y. Yang, W.-J. Zhang, H. Li, Y. Li, X. Jiang, L. Gan, G. Yang, L. You, Z. Wang *et al.*, *Science* **370**, 1460 (2020).
- [11] I. Bloch, *Nature (London)* **453**, 1016 (2008).
- [12] F. Schäfer, T. Fukuhara, S. Sugawa, Y. Takasu, and Y. Takahashi, *Nat. Rev. Phys.* **2**, 411 (2020).
- [13] C. Nayak, S. H. Simon, A. Stern, M. Freedman, and S. Das Sarma, *Rev. Mod. Phys.* **80**, 1083 (2008).
- [14] T. D. Ladd, F. Jelezko, R. Laflamme, Y. Nakamura, C. Monroe, and J. L. O'Brien, *Nature (London)* **464**, 45 (2010).
- [15] J. I. Cirac and P. Zoller, *Phys. Rev. Lett.* **74**, 4091 (1995).
- [16] P. Wang, C.-Y. Luan, M. Qiao, M. Um, J. Zhang, Y. Wang, X. Yuan, M. Gu, J. Zhang, and K. Kim, *Nat. Commun.* **12**, 233 (2021).
- [17] T. P. Harty, D. T. C. Allcock, C. J. Ballance, L. Guidoni, H. A. Janacek, N. M. Linke, D. N. Stacey, and D. M. Lucas, *Phys. Rev. Lett.* **113**, 220501 (2014).
- [18] A. H. Myerson, D. J. Szwer, S. C. Webster, D. T. C. Allcock, M. J. Curtis, G. Imreh, J. A. Sherman, D. N. Stacey, A. M. Steane, and D. M. Lucas, *Phys. Rev. Lett.* **100**, 200502 (2008).
- [19] C. J. Ballance, T. P. Harty, N. M. Linke, M. A. Sepiol, and D. M. Lucas, *Phys. Rev. Lett.* **117**, 060504 (2016).
- [20] J. P. Gaebler, T. R. Tan, Y. Lin, Y. Wan, R. Bowler, A. C. Keith, S. Glancy, K. Coakley, E. Knill, D. Leibfried, and D. J. Wineland, *Phys. Rev. Lett.* **117**, 060505 (2016).
- [21] C. R. Clark, H. N. Tinkey, B. C. Sawyer, A. M. Meier, K. A. Burkhardt, C. M. Seck, C. M. Shappert, N. D. Guise, C. E. Volin, S. D. Fallek, H. T. Hayden, W. G. Rellergert, and K. R. Brown, *Phys. Rev. Lett.* **127**, 130505 (2021).
- [22] P. Schindler, J. T. Barreiro, T. Monz, V. Nebendahl, D. Nigg, M. Chwalla, M. Hennrich, and R. Blatt, *Science* **332**, 1059 (2011).
- [23] T. Monz, D. Nigg, E. A. Martinez, M. F. Brandl, P. Schindler, R. Rines, S. X. Wang, I. L. Chuang, and R. Blatt, *Science* **351**, 1068 (2016).
- [24] S. Gulde, M. Riebe, G. P. T. Lancaster, C. Becher, J. Eschner, H. Häffner, F. Schmidt-Kaler, I. L. Chuang, and R. Blatt, *Nature (London)* **421**, 48 (2003).
- [25] A. Sørensen and K. Mølmer, *Phys. Rev. Lett.* **82**, 1971 (1999).
- [26] K. Mølmer and A. Sørensen, *Phys. Rev. Lett.* **82**, 1835 (1999).
- [27] A. Sørensen and K. Mølmer, *Phys. Rev. A* **62**, 022311 (2000).
- [28] C. Monroe and J. Kim, *Science* **339**, 1164 (2013).
- [29] S.-L. Zhu, C. Monroe, and L.-M. Duan, *Europhys. Lett.* **73**, 485 (2006).
- [30] S.-L. Zhu, C. Monroe, and L.-M. Duan, *Phys. Rev. Lett.* **97**, 050505 (2006).
- [31] G.-D. Lin, S.-L. Zhu, R. Islam, K. Kim, M.-S. Chang, S. Korenblit, C. Monroe, and L.-M. Duan, *Europhys. Lett.* **86**, 60004 (2009).
- [32] Y. Wu, S.-T. Wang, and L.-M. Duan, *Phys. Rev. A* **97**, 062325 (2018).

- [33] P. H. Leung, K. A. Landsman, C. Figgatt, N. M. Linke, C. Monroe, and K. R. Brown, *Phys. Rev. Lett.* **120**, 020501 (2018).
- [34] Y. Wang, S. Crain, C. Fang, B. Zhang, S. Huang, Q. Liang, P. H. Leung, K. R. Brown, and J. Kim, *Phys. Rev. Lett.* **125**, 150505 (2020).
- [35] M. Kang, Q. Liang, B. Zhang, S. Huang, Y. Wang, C. Fang, J. Kim, and K. R. Brown, *Phys. Rev. Appl.* **16**, 024039 (2021).
- [36] A. R. Milne, C. L. Edmunds, C. Hempel, F. Roy, S. Mavadia, and M. J. Biercuk, *Phys. Rev. Appl.* **13**, 024022 (2020).
- [37] T. J. Green and M. J. Biercuk, *Phys. Rev. Lett.* **114**, 120502 (2015).
- [38] Y. Lu, S. Zhang, K. Zhang, W. Chen, Y. Shen, J. Zhang, J.-N. Zhang, and K. Kim, *Nature (London)* **572**, 363 (2019).
- [39] P. H. Leung and K. R. Brown, *Phys. Rev. A* **98**, 032318 (2018).
- [40] K. A. Landsman, Y. Wu, P. H. Leung, D. Zhu, N. M. Linke, K. R. Brown, L. Duan, and C. Monroe, *Phys. Rev. A* **100**, 022332 (2019).
- [41] B. Reinhold, G. Nikodem, P. Neal, K. Wright, and Y. Nam, *npj Quantum Inf* **7**, 147 (2021).
- [42] Y. Shapira, R. Shaniv, T. Manovitz, N. Akerman, L. Peleg, L. Gazit, R. Ozeri, and A. Stern, *Phys. Rev. A* **101**, 032330 (2020).
- [43] T. Choi, S. Debnath, T. A. Manning, C. Figgatt, Z.-X. Gong, L. -M. Duan, and C. Monroe, *Phys. Rev. Lett.* **112**, 190502 (2014).
- [44] S. Debnath, N. M. Linke, C. Figgatt, K. A. Landsman, K. Wright, and C. Monroe, *Nature (London)* **536**, 63 (2016).
- [45] C. Figgatt, A. Ostrander, N. M. Linke, K. A. Landsman, D. Zhu, D. Maslov, and C. Monroe, *Nature (London)* **572**, 368 (2019).
- [46] R. Blümel, N. Grzesiak, N. H. Nguyen, A. M. Green, M. Li, A. Maksymov, N. M. Linke, and Y. Nam, *Phys. Rev. Lett.* **126**, 220503 (2021).
- [47] S. R. Bastin and T. E. Lee, *J. Appl. Phys.* **121**, 014312 (2017).
- [48] M.-S. Li, X.-X. Rao, Z. Wang, P.-F. Lu, F. Zhu, Y. Liu, and L. Luo, *Quantum Inf. Process.* **21**, 65 (2022).
- [49] D. F. V. James, *Appl. Phys. B* **66**, 181 (1998).
- [50] H. Landa, M. Drewsen, B. Reznik, and A. Retzker, *New J. Phys.* **14**, 093023 (2012).
- [51] P. C. Haljan, K.-A. Brickman, L. Deslauriers, P. J. Lee, and C. Monroe, *Phys. Rev. Lett.* **94**, 153602 (2005).
- [52] P. J. Lee, K.-A. Brickman, L. Deslauriers, P. C. Haljan, L.-M. Duan, and C. Monroe, *J. Opt. B: Quantum Semiclass. Opt.* **7**, S371 (2005).
- [53] K. Wright, K. M. Beck, S. Debnath, J. M. Amini, Y. Nam, N. Grzesiak, J.-S. Chen, N. C. Pienta, M. Chmielewski, C. Collins, K. M. Hudek, J. Mizrahi, J. D. Wong-Campos, S. Allen, J. Apisdorf, P. Solomon, M. Williams, A. M. DuCore, A. Blinov, S. M. Kreikemeier *et al.*, *Nat. Commun.* **10**, 5464 (2019).